



## Hyporheic flow and residence time distributions in heterogeneous cross-bedded sediment

Audrey Hucks Sawyer<sup>1</sup> and M. Bayani Cardenas<sup>1</sup>

Received 2 December 2008; revised 4 May 2009; accepted 21 May 2009; published 7 August 2009.

[1] The permeability heterogeneity of cross-bedded sediment increases path lengths of river-groundwater mixing (hyporheic exchange) in riverbeds and modifies the distribution of residence times. For two case studies, we numerically simulated fluid flow and solute transport through immobile bed forms composed of heterogeneous sediment and equivalent homogeneous sediment in order to clarify how cross-bedded permeability structures impact hyporheic exchange. The two permeability fields are from the cross-bedded Massillon Sandstone and modern climbing ripple deposits of the Brazos River (Texas). In both cases, permeability heterogeneity creates long hyporheic exchange paths but only slightly increases the depth of exchange relative to equivalent homogeneous sediment. In the Massillon example, permeability heterogeneity increases the proportion of long hyporheic residence times (>3 days). In the Brazos example, permeability heterogeneity increases the proportion of short residence times (<17 h). We attribute the different responses in residence time distributions to differences in permeability patterns near the sediment-water interface. The tails of residence time distributions extend for tens of years and conform to a power law in both heterogeneous and homogeneous sediment. Current-bed form interactions are responsible for the long tails, as opposed to permeability heterogeneity.

**Citation:** Sawyer, A. H., and M. B. Cardenas (2009), Hyporheic flow and residence time distributions in heterogeneous cross-bedded sediment, *Water Resour. Res.*, 45, W08406, doi:10.1029/2008WR007632.

### 1. Introduction

[2] The riverbed is an important interface between surface water and groundwater. Fluid flow across the riverbed transports solutes and energy between aquatic and riparian ecosystems. River water infiltrates into the bed and banks, travels along short groundwater flow paths, and returns to the channel. The resulting near-channel zone of surface water-groundwater mixing is the hyporheic zone, a critical ecological transition zone [Brunke and Gonser, 1997; Stanford and Ward, 1988]. Hyporheic flow occurs over a wide range of spatial scales (from bed form to catchment) and temporal scales (from minutes to weeks). As water flows through the hyporheic zone, time-dependent microbial reactions transform its chemical composition. The residence time of water in the hyporheic zone therefore determines concentrations of both nutrients and contaminants within the sediment and surface water [Haggerty *et al.*, 2002].

[3] Riverbed topography strongly influences hyporheic residence times and path lengths. An undulating riverbed deflects currents, creating pressure gradients along the sediment-water interface that drive hyporheic exchange. Ripples, dunes, pools, steps, and riffles drive relatively short hyporheic flow paths [Cardenas, 2007; Elliott and Brooks, 1997b; Harvey and Bencala, 1993; Hester and

Doyle, 2008; Thibodeaux and Boyle, 1987], while meanders promote longer paths [Boano *et al.*, 2006; Peterson and Sickbert, 2006]. Studies that characterize hyporheic exchange through bed forms and planforms typically assume the sediment is homogeneous for simplicity [i.e., Boano *et al.*, 2006; Cardenas and Wilson, 2007; Elliott and Brooks, 1997a, 1997b; Harvey and Bencala, 1993; Worman *et al.*, 2006].

[4] Permeability heterogeneity in riverbed sediment also drives hyporheic exchange by deflecting flow downward into the sediment or upward into the channel [Vaux, 1968]. Permeability heterogeneity should therefore alter hyporheic exchange paths and residence times in bed forms and planforms, but few studies have quantified its influence. Salehin *et al.* [2004] constructed bed forms on top of a gridded, three-dimensional, lognormally correlated random permeability field in a flume and monitored hyporheic exchange through the sediment. Permeability heterogeneity reduced hyporheic exchange residence times and penetration depths. How their results transfer to natural sedimentary deposits is uncertain. Marion *et al.* [2008] developed an analytical solution for the impact of horizontally layered permeability fields on hyporheic exchange and validated their solution with flume experiments. They showed that the proportion of short hyporheic residence times (~1 min) increases in sediment with a highly permeable armored layer. Cardenas *et al.* [2004] numerically simulated hyporheic exchange through heterogeneous channel bend deposits. Their sensitivity analysis demonstrated that permeability heterogeneity with large variance and long correlation ranges can dominate hyporheic exchange in rivers.

<sup>1</sup>Department of Geological Sciences, University of Texas at Austin, Austin, Texas, USA.

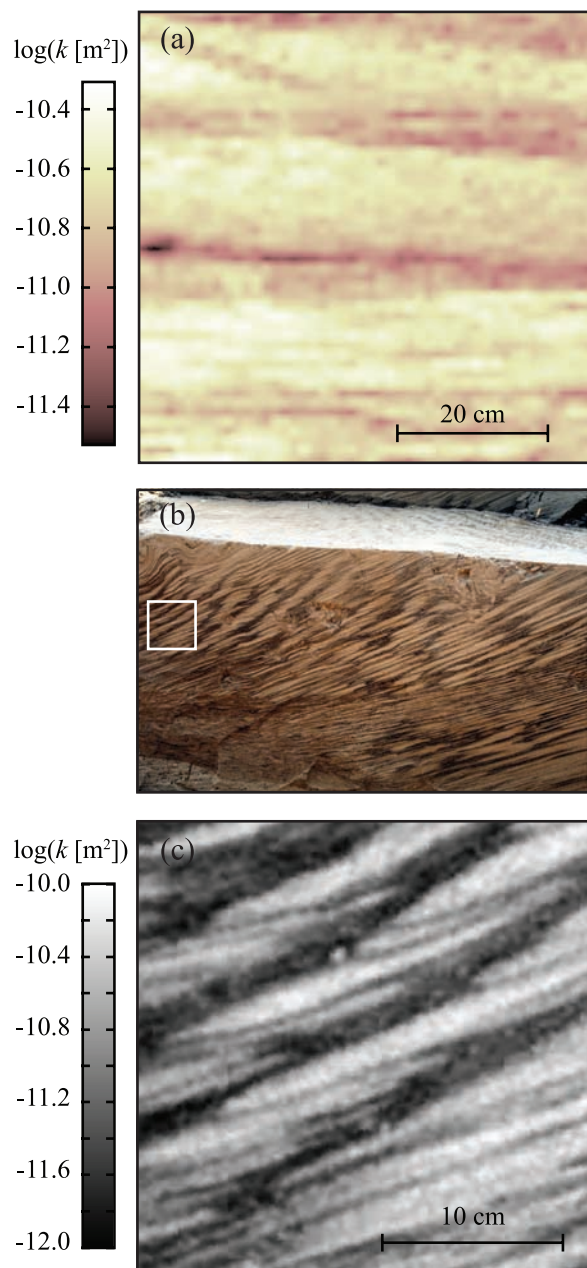


**Figure 1.** Permeability data sets. (a) Direct permeability measurements by *Tidwell and Wilson* [2000, 2002] on the cross-bedded Massillon Sandstone. (b) Photograph of modern climbing ripple deposits excavated from a point bar of the Brazos River, Texas, courtesy of Gary Kocurek (University of Texas at Austin). White box delineates region used in image analysis. (c) Permeability field from image analysis. Less permeable zones are associated with dark organic-rich silt. More permeable zones are associated with clean fine sand.

However, their study only considered one permeability field with large (meter scale) correlation lengths. *Boano et al.* [2007] presented a model for solute transport and storage in rivers with heterogeneous bed form sizes and sediment permeability. They limited their analysis to fine permeability variations with a correlation length much less than the mean bed form wavelength.

[5] The hierarchy of sedimentary units within fluvial deposits produces a hierarchy of permeability structures, from microform scale (laminations) to mesoform scale (crossbed sets) to macroform scale (point bar assemblages) [*Ritzi et al.*, 2004]. *Cardenas et al.* [2004] described how macroscale permeability variations influence hyporheic exchange, while *Boano et al.* [2007] described the influence of microscale variations. To our knowledge, no study has tested the influence of mesoscale permeability variations on hyporheic exchange. This scale is relevant for two reasons. First, the depth of hyporheic exchange and the size of mesoforms both scale with bed form size. We interpret that hyporheic flow paths often encounter mesoforms such as cross beds that could influence the exchange. Unfortunately, mesoscale permeability heterogeneity is difficult if not impossible to measure in riverbeds or flumes, so previous studies have ignored its influence on hyporheic exchange. Second, evidence suggests that permeability and grain size variations impact the ecological health and structure of hyporheic fauna and salmonid species, even at relatively small scales [*Boulton*, 2007; *Greig et al.*, 2007; *Hakenkamp et al.*, 2002; *Wagner and Bretschko*, 2002].

[6] The goal of this study is to quantify how the permeability structure of mesoforms such as cross beds influences hyporheic exchange. For two case studies, we numerically simulate hyporheic exchange through immobile bed forms with cross-bedded permeability structures. In each case, we estimate the equivalent homogeneous permeability of the sediment and simulate hyporheic exchange in the homogeneous medium for comparison. We show that cross-bedded permeability structures do impact hyporheic exchange paths, but average exchange depths and fluxes are similar in heterogeneous and equivalent homogeneous sediment. While the permeability variations also impact the distribution of residence times, all distributions have power law tails. This important result implies that solute residence times span many orders of magnitude, regardless of permeability structure.

## 2. Methods

### 2.1. Permeability Data Sets

[7] The Massillon Sandstone data set consists of high-resolution, direct permeability measurements. Using a gas minipermeameter, *Tidwell and Wilson* [2000, 2002] acquired 2500 permeability measurements at intervals of 1.27 cm on a two-dimensional face of the Massillon Sandstone (Figure 1a). They used a minipermeameter tip seal with inner radius of 0.31 cm, which suggests the measurement support volume was on the order of a cubic centimeter. To our knowledge, this data set represents the most detailed permeability map generated directly from cross-bedded sediment. Because diagenetic alterations have likely decreased the permeability of the Massillon Sandstone [*Tidwell and Wilson*, 2002], we uniformly scaled the permeability field by a factor of 10. The average scaled permeability is  $1.8 \times 10^{-11} \text{ m}^2$ , typical of clean sand [*Freeze and Cherry*, 1979] (Figure 1a).

[8] We also developed a second permeability field from an image of climbing ripple deposits excavated within a point bar of the Brazos River near Wallis, Texas (Figures 1b and 1c). The bimodal deposits are composed of clean sand,

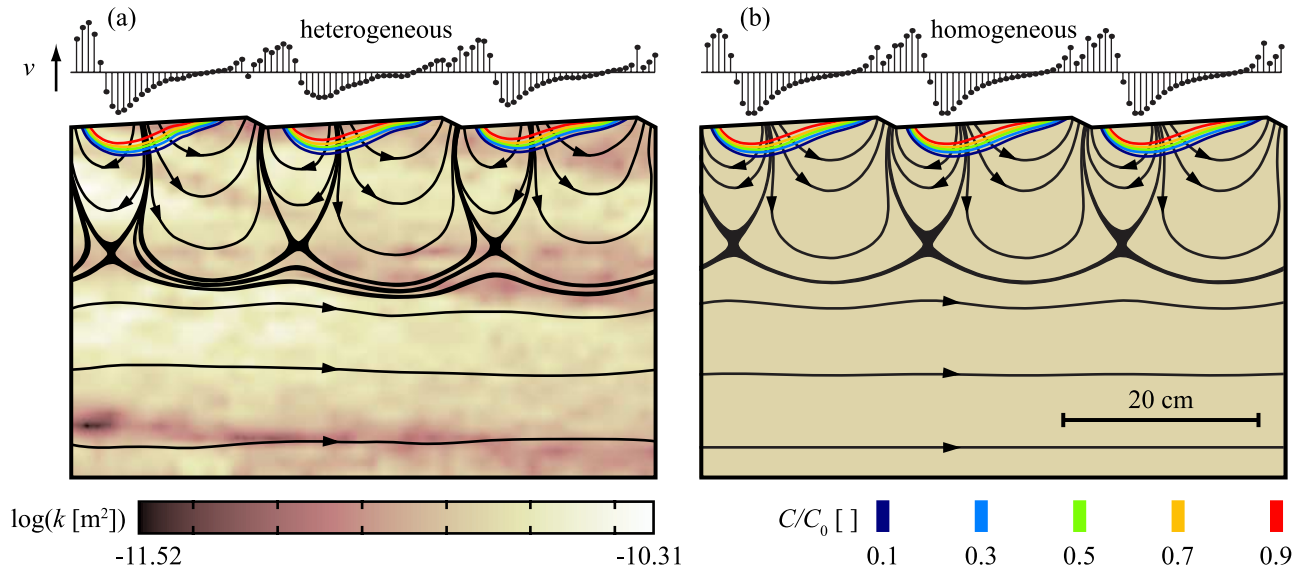


**Figure 2.** Simulated hyporheic exchange in (a) heterogeneous Massillon Sandstone and (b) equivalent homogeneous sediment. Flow in the channel is left to right. Streamlines are shown in black. Normalized seepage velocity across the sediment-water interface is plotted above the bed forms. The hyporheic zone is slightly deeper in heterogeneous sediment. Color contours indicate normalized solute concentrations ( $C/C_0$ ) 12 h after introduction of a conservative solute to the surface water.

which appears lighter in photograph, and dark organic-rich silt, which appears darker in photograph (Figure 1b). *Tidwell and Wilson* [2002] showed that images can be used to delineate spatial permeability patterns where direct measurements are lacking, especially in rocks with sharp permeability transitions. Owing to the difficulty of obtaining high-resolution permeability measurements in unlithified sediment, we assumed a relationship between image gray scale values and permeability. Specifically, we normalized gray scale values between zero and one and linearly translated them to log-permeability values between  $-10$  and  $-12$ . As a result, the permeability of dark silt is approximately  $10^{-12} \text{ m}^2$ , and the permeability of light sand is approximately  $10^{-10} \text{ m}^2$  [*Freeze and Cherry, 1979*].

## 2.2. Geostatistical Analysis

[9] To describe the spatial correlation of permeability, we report semivariogram models for the log-permeability data. *Tidwell and Wilson* [2000] computed experimental and model semivariograms for the Massillon data. For the Brazos data, we computed experimental and model semivariograms using GSLIB [*Deutsch and Journel, 1998*]. The experimental semivariogram,  $\gamma(\underline{h})$ , is half the average squared difference between two attribute values,  $y(\underline{u}_i)$  and  $y(\underline{u}_i + \underline{h})$ , separated by lag vector  $\underline{h}$ :

$$\gamma(\underline{h}) = \frac{1}{2n(\underline{h})} \sum_{i=1}^{n(\underline{h})} (y(\underline{u}_i) - y(\underline{u}_i + \underline{h}))^2, \quad (1)$$

where  $n(\underline{h})$  is the number of pairs [*Deutsch and Journel, 1998*]. The model semivariogram is composed of  $p$  semivariogram structures:

$$\gamma(\underline{h}) = \sum_{i=1}^p c_i \Gamma_i \left( \frac{\underline{h}}{a_i} \right), \quad (2)$$

where each semivariogram structure ( $\Gamma_i$ ) is defined by its shape, semivariance contribution ( $c_i$ ), and range ( $a_i$ ). Mathematical forms for spherical, exponential, and hole structures are available in the work of *Deutsch and Journel* [1998].

## 2.3. Estimating an Equivalent Homogeneous Permeability Tensor

[10] For both the Massillon and Brazos permeability fields, we estimated an equivalent homogeneous permeability tensor using the method of *Durlofsky* [1991]. The numerical method mimics two constant-head permeameter tests in orthogonal directions. For each direction, steady flow is simulated across the heterogeneous permeability field. In the first simulation, left and right boundaries are spatially periodic in head drop, while top and bottom boundaries are spatially periodic in head. In the second simulation, the boundary conditions are rotated such that the sides have periodic head, and the top and bottom have a periodic head drop. Periodic boundary conditions ensure a symmetrical equivalent permeability tensor [*Durlofsky, 1991; Renard and de Marsily, 1997*]. The four components of the equivalent permeability tensor are obtained from mean fluxes across the two pairs of periodic boundaries in the two simulations.

## 2.4. Hyporheic Flow and Solute Transport Simulations

[11] In simulations with heterogeneous permeability fields, we shaped the top of the domain to resemble repeating bed forms (i.e., Figure 2a). Two criteria guided our choice of bed form wavelength. We maximized the number of bed forms within the computational domain while maintaining a bed form wavelength on the order of the permeability correlation length. In the Massillon case study, the bed form wavelength is 20 cm (one third of the width of the permeability field). We vertically positioned the bed form troughs within a low-permeability bounding

**Table 1.** Numerical Simulation Parameters

	Massillon Sandstone	Brazos Sediment	Homogeneous Anisotropic Sediment
Mean hydraulic gradient, $S$ (mm m <sup>-1</sup> )	.194	.149	.095
Mean channel velocity (m s <sup>-1</sup> )	0.10	0.10	0.10
Reynolds number (dimensionless)	20,000	20,000	50,000
Bedform wavelength, $\lambda$ (m)	0.2	0.1	1.0
Bedform height (m)	0.01	0.005	0.05
Porosity (dimensionless)	0.3	0.3	0.3
Dynamic viscosity, $\mu$ (Pa s)	0.001	0.001	0.001
Longitudinal dispersivity, $\alpha_L$ (mm)	1	1	5
Transverse dispersivity, $\alpha_T$ (mm)	0.1	0.1	0.5
Molecular diffusion coefficient, $D'_m$ (m <sup>2</sup> s <sup>-1</sup> )	$5 \times 10^{-11}$	$5 \times 10^{-11}$	$5 \times 10^{-11}$

surface. This configuration implies that the bed form train truncated the underlying cross beds. In the Brazos case study, the bed form wavelength is 10 cm, which is the approximate horizontal length scale of repeating permeability patterns. We laterally positioned the bed form troughs in less permeable zones. This configuration implies that the troughs of climbing ripples preferentially trapped finer sediment. In all simulations, the bed form height-to-wavelength ratio is 0.05, and the lee slope is 27°.

[12] Using both heterogeneous and equivalent homogeneous permeability fields, we simulated hyporheic flow through bed forms following the method of *Cardenas and Wilson* [2007]. Turbulent flow over repeating bed forms and porous flow within the sediment are linked through the pressure distribution at the sediment-water interface [see *Cardenas and Wilson*, 2007, Figure 1]. First, two-dimensional steady state turbulent flow over impermeable periodic bed forms is solved using the steady state Reynolds-averaged Navier-Stokes (RANS) equations with the  $k - \omega$  closure scheme. The sediment-water interface is a no-slip boundary, and the top of the water column is a symmetry boundary. Side boundaries are spatially periodic with a prescribed potential drop representative of the channel slope. Detailed discussion of the methodology, turbulent flow behavior, and model validation are available in the work of *Cardenas and Wilson* [2007].

[13] Next, two-dimensional porous flow in sediment is solved using the steady state groundwater flow equation:

$$\nabla \cdot \left( -\frac{\underline{k}}{\mu} \nabla P \right) = 0, \quad (3)$$

where  $\underline{k}$  is the full permeability tensor,  $\mu$  is viscosity, and  $P$  is total potential (the sum of static, dynamic, and elevation components). The sediment-water interface is assigned the total potential gradient from the turbulent channel flow simulation. The base of the porous flow domain is a no-flow boundary, and the left and right sides are spatially periodic boundaries with a potential drop representative of the channel slope.

[14] Porous fluid flow simulations provide the velocity field for transient solute transport simulations. The advection-

diffusion-dispersion equation describes solute transport in porous sediment:

$$\frac{\partial C}{\partial t} = -\nabla \cdot (\underline{v}C) + \nabla \cdot (\underline{D}\nabla C), \quad (4)$$

where  $C$  is concentration,  $t$  is time, and  $\underline{v}$  is seepage velocity (specific discharge divided by porosity), which has components  $v_x$  and  $v_z$ .  $\underline{D}$  is the full mechanical dispersion tensor with components:

$$D_{xx} = \alpha_L \frac{v_x^2}{|v|} + \alpha_T \frac{v_z^2}{|v|} + D'_m, \quad (5a)$$

$$D_{xz} = D_{zx} = (\alpha_L - \alpha_T) \frac{v_x v_z}{|v|}, \quad (5b)$$

$$D_{zz} = \alpha_L \frac{v_z^2}{|v|} + \alpha_T \frac{v_x^2}{|v|} + D'_m. \quad (5c)$$

Transverse and longitudinal dispersivities are  $\alpha_T$  and  $\alpha_L$ , and  $D'_m$  is the molecular diffusion coefficient in porous media. In all simulations, the porosity is 0.30,  $D'_m$  is  $5 \times 10^{-11}$  m<sup>2</sup> s<sup>-1</sup>, and  $\alpha_T$  is 1/10 of  $\alpha_L$  (Table 1). To represent pore scale dispersion,  $\alpha_L$  is approximately several grain diameters. We did not include macroscopic dispersivity in any simulation. Macroscopic dispersion accounts for the bulk effect of permeability heterogeneity on solute transport. In heterogeneous simulations, the permeability field is known, and macroscopic dispersion would “double-count” the influence of permeability heterogeneity. In homogeneous simulations, our goal was to simulate solute transport in truly homogeneous sediment for comparison with heterogeneous simulations.

[15] Solute transport simulations mimic penetration of river water with constant conservative solute concentration ( $C_0$ ) into the hyporheic zone [*Cardenas et al.*, 2008]. Initial solute concentration in the sediment is zero. Along the sediment-water interface, downwelling zones have a constant normalized concentration ( $C/C_0$ ) of 1.0. Upwelling zones are convective flux boundaries. The model sides are periodic concentration boundaries, and the base is a convective flux boundary. Solute breakthrough curves are

**Table 2.** Semivariogram Model Properties for Massillon and Brazos Permeability Data<sup>a</sup>

$c$	Structure	$a_{\text{maj}}$ (m)/Dip ( $^{\circ}$ )	$a_{\text{min}}$ (m)
<i>Massillon Sandstone</i>			
.011	exponential	.04	.04
.043	exponential	.348/0	.195
.012	hole	$\infty/0$	.18
<i>Brazos Sediment</i>			
.012	spherical	.04	.04
.007	spherical	.14	.14
.013	spherical	$\infty/59$	.14
.024	hole <sup>b</sup>	$\infty/-31$	.050

<sup>a</sup>Downstream dips are positive, and upstream dips are negative.

<sup>b</sup>We used a damped hole effect structure with a decay parameter of  $1.6 \times 10^6$ . The decay parameter represents the distance over which the sinusoidal variance contribution decays by 95%.

calculated as the flux-weighted normalized mean upwelling concentration ( $C_u/C_0$ ). At each time step, the flux-weighted concentration is integrated over upwelling boundaries and divided by the flux-weighted concentration integrated over downwelling boundaries. The residence time distribution is the time derivative of the normalized flux-weighted breakthrough curve.

[16] The RANS equations are solved using the finite volume approach implemented in FLUENT [Fluent Inc., 2006]. We checked for grid dependence by repeating simulations with refined meshes. The groundwater flow and solute transport equations are solved using the finite element approach in COMSOL Multiphysics [COMSOL AB, 2006]. The sediment domain consists of Lagrange quadratic triangular elements with node spacing of less than 1 mm at the top and less than 5 mm at the base. We tested for mesh dependence and positioned the basal boundary sufficiently far from the hyporheic zone to eliminate its influence on the solution.

### 3. Massillon Sandstone: A Cross-Bedded Sand Case Study

#### 3.1. Lithology

[17] The Massillon Sandstone (Pennsylvanian age) is a moderately well sorted, medium-grained quartz sandstone. Cross-stratified sets are 16–22 cm in thickness and are bounded by subhorizontal, undulatory to planar surfaces (Figure 1a). Within each set, unidirectional laminae are 0.5–2.0 cm thick and have apparent dips from  $10^{\circ}$  to  $22^{\circ}$ . Evidence of diagenetic alteration includes hydrous iron oxide precipitates and quartz overgrowths [Tidwell and Wilson, 2000, 2002]. The depositional environment has been interpreted as high-energy fluvial or tidal [Gray, 1956; Schmidley, 1986].

#### 3.2. Geostatistical Properties

[18] Permeability values range by 1.2 orders of magnitude, and the geometric mean permeability is  $1.8 \times 10^{-11}$  m<sup>2</sup>. The semivariogram of the log-permeability field exhibits three nested structures: a small-scale structure associated with low-angle laminae, a large-scale structure associated with cross bed sets, and a periodic “hole” structure associated with the repetition of less permeable bounding surfaces [see Tidwell and Wilson, 2000, Figure 7] (Table

2). The longest spatial correlation is in the direction parallel to bounding surfaces (nearly horizontal) [Tidwell and Wilson, 2000].

#### 3.3. Hyporheic Flow and Transport in Heterogeneous Medium

[19] The average hyporheic exchange depth over the three bed forms is 16.9 cm, calculated as the hyporheic exchange area divided by domain width. The average exchange depth is 84% of the bed form wavelength. The hyporheic exchange zone exhibits complex flow paths of varying length (Figure 2a). Shorter exchange paths enter the hyporheic zone at the stoss face of one bed form and return to the channel at an adjacent upwelling zone. These exchange paths represent approximately 89% of the total exchange area. The remaining exchange paths are significantly longer because they connect nonadjacent upwelling and downwelling zones on different bed forms. The average hyporheic exchange flux across the sediment-water interface is  $7.12 \times 10^{-8}$  m s<sup>-1</sup>. The characteristic hyporheic residence time, calculated as the average hyporheic depth divided by the average exchange flux, is 27.4 days.

#### 3.4. Hyporheic Flow and Transport in Homogeneous Medium

[20] The Massillon Sandstone has an equivalent anisotropy ratio ( $k_{\text{max}}/k_{\text{min}}$ ) of 1.09, with a maximum permeability ( $k_{\text{max}}$ ) of  $2.07 \times 10^{-11}$  m<sup>2</sup> that dips  $1.3^{\circ}$  downstream. The maximum permeability direction is parallel to subhorizontal bounding surfaces (Figure 1). The average hyporheic exchange depth across the three bed forms is 15.0 cm, which is slightly less than the exchange depth in the heterogeneous medium (Figure 2). Unlike in heterogeneous sediment, hyporheic flow paths only connect adjacent upwelling and downwelling zones (Figure 2b). The average hyporheic exchange flux across the sediment-water interface is  $8.92 \times 10^{-8}$  m s<sup>-1</sup>, which is greater than the exchange flux in heterogeneous sediment. The characteristic hyporheic residence time is 19.8 days, which is less than in heterogeneous sediment.

[21] Figure 3 compares the conservative solute breakthrough curves and residence time distributions for heterogeneous and homogeneous sediment. The breakthrough curve initially climbs faster in homogeneous sediment.  $C_u/C_0$  reaches 50% after 36 h in homogeneous sediment and after 50 h in heterogeneous sediment. Accordingly, the homogeneous sediment has a greater proportion of residence times less than  $3 \times 10^5$  s (3 days), while the heterogeneous sediment has a greater proportion of residence times greater than  $3 \times 10^5$  s. Both residence time distributions have power law tails that end at a maximum residence time of approximately 30 years ( $\sim 10^9$  s).

### 4. Brazos River Sediment: A Climbing Ripple Case Study

#### 4.1. Lithologic Description

[22] The Brazos River sediment is ripple laminated and bimodal in composition. The modes are fine sand and organic-rich silt. Over the entire exposure (approximately one meter in thickness), the angle of ripple climb steepens from  $15^{\circ}$  near the base to  $40^{\circ}$  near the top (Figure 1b). The transport dynamics associated with ripple formation and

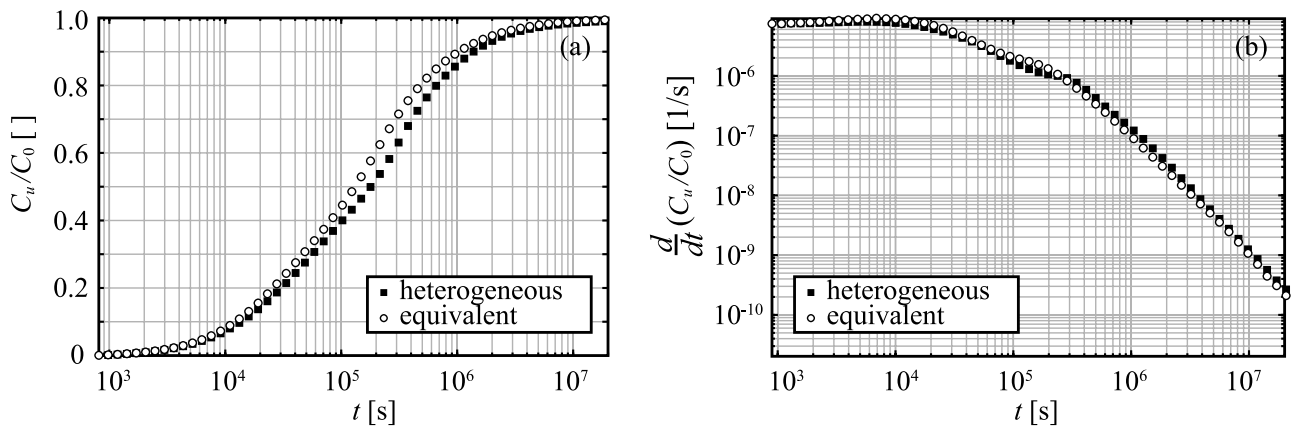


**Figure 3.** (a) Breakthrough curves for the heterogeneous Massillon Sandstone (black squares) and its homogeneous equivalent sediment (white circles). The breakthrough curve initially climbs faster in homogeneous sediment. (b) Residence time distributions for heterogeneous and homogeneous sediment. Both distributions have power law tails with exponents of  $-1.92$ .

migration typically create local grain size patterns. Often, the finest sediment is located on ripple stoss faces, while the coarsest sediment is located on lee faces [Allen, 1971]. However, the inverse can also occur, where suspended silts become trapped and deposited in recirculation zones behind ripple crests. In this case, the coarsest sediment is preserved on ripple stoss faces updip of eddy reattachment points, while fine sediment is deposited on lee faces and in ripple swales. In the Brazos River sediment, we interpret the darker silt as the preserved ripple swales and the lighter sand as the preserved upper stoss faces.

**4.2. Geostatistical Properties**

[23] The geometric mean permeability of the Brazos data set is  $1.2 \times 10^{-11} \text{ m}^2$ . The experimental semivariogram of log-permeabilities exhibits four nested structures (Figure 4 and Table 2). Alignment of sand and silt lenses gives rise to a periodic “hole” structure with a range of 5 cm perpendicular to the direction of climb (Figure 4b). The other structures include a small-scale spherical structure with a range of 4 cm and a large-scale spherical structure with a range of 14 cm (Figure 4a). The experimental semivario-

gram exhibits zonal anisotropy at the large scale, with a greater variance contribution parallel to ripple climb (Table 2).

**4.3. Hyporheic Flow and Transport in Heterogeneous Medium**

[24] The average hyporheic exchange depth within heterogeneous sediment is 9.9 cm (99% of the bed form wavelength). Like the Massillon Sandstone, the Brazos sediment contains deep flow paths that connect nonadjacent bed forms (Figure 5a). The shallow exchange zones, which connect adjacent downwelling and upwelling regions, represent approximately 63% of the total exchange area. The average hyporheic exchange flux across the sediment-water interface is  $7.87 \times 10^{-8} \text{ m s}^{-1}$ . The characteristic hyporheic residence time is 14.5 days.

**4.4. Hyporheic Flow and Transport in Homogeneous Medium**

[25] The Brazos sediment has an equivalent anisotropy ratio of 1.66, with a maximum permeability of  $1.53 \times 10^{-11} \text{ m}^2$  that dips  $29.2^\circ$  upstream. The direction of maximum

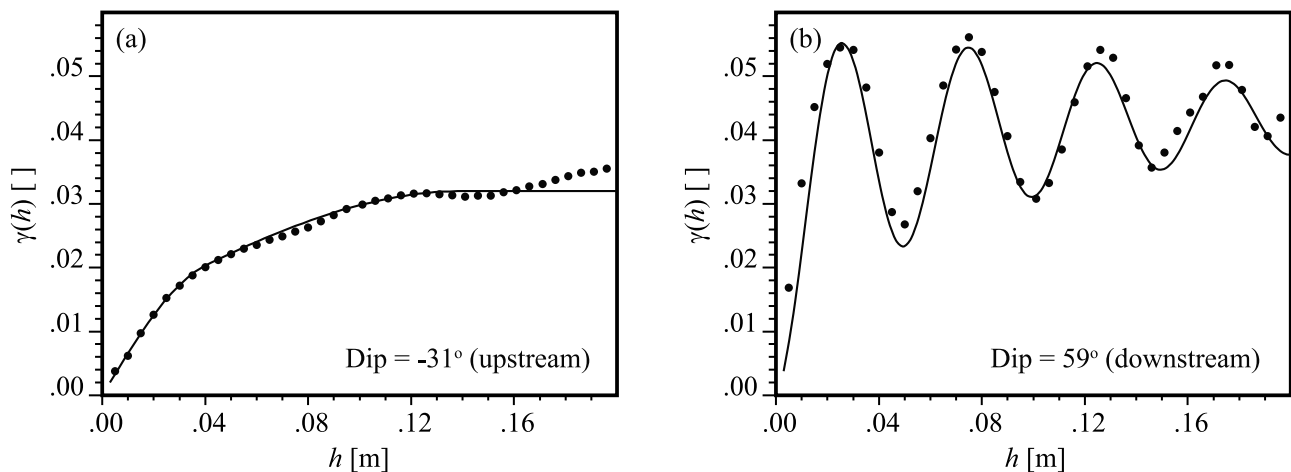


**Figure 4.** Experimental and model semivariograms for Brazos log-permeability values (a) parallel to ripple climb and (b) perpendicular to climb. The semivariogram oscillates in the  $59^\circ$  dip direction owing to the alternation of sand and silt bands.

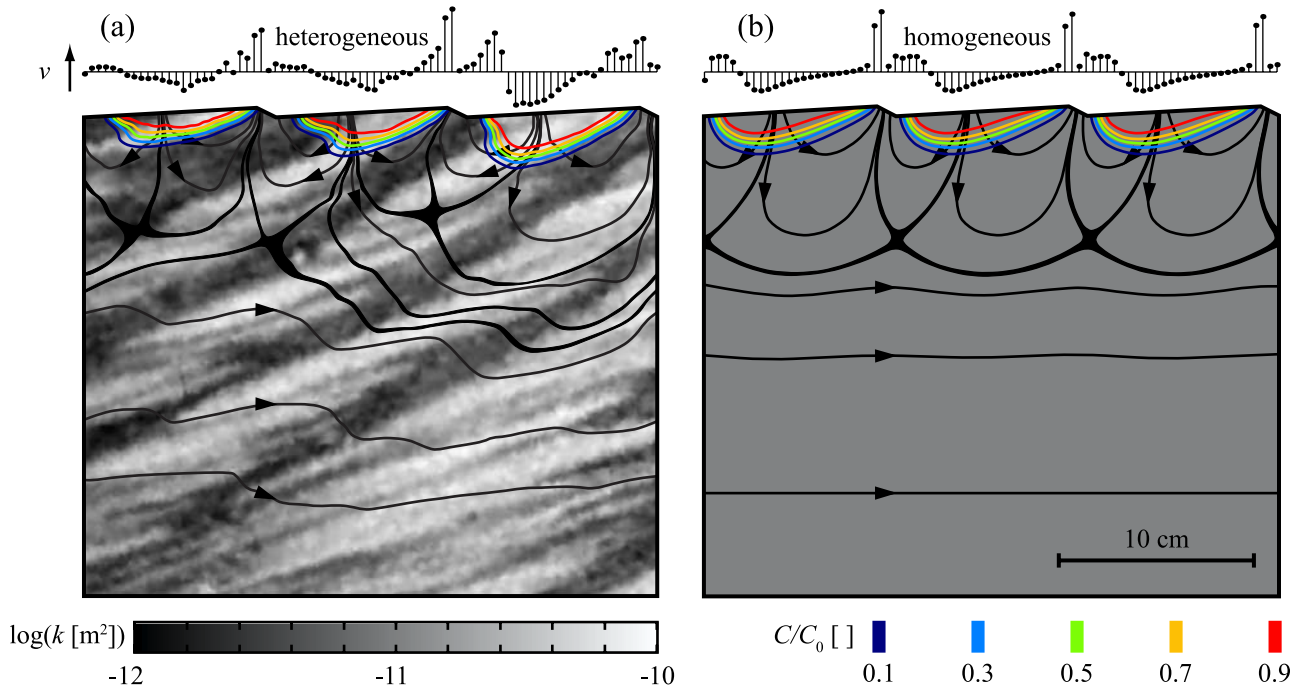


**Figure 5.** Simulated hyporheic exchange in (a) heterogeneous Brazos sediment and (b) equivalent homogeneous sediment. Flow in the channel is left to right. Streamlines are shown in black. Normalized seepage velocity across the sediment-water interface is plotted above the bed forms. The hyporheic zone is deeper in heterogeneous sediment. Color contours indicate normalized solute concentrations ( $C/C_0$ ) 12 h after introduction of a conservative solute to the surface water.

permeability is parallel to the angle of climb (Figure 1c). The average hyporheic exchange depth across the three bed forms is 8.0 cm, which is less than the exchange depth in the heterogeneous medium. Hyporheic exchange paths only connect adjacent downwelling and upwelling zones (Figure 5b). The average hyporheic exchange flux across the sediment-water interface is  $6.40 \times 10^{-8} \text{ m s}^{-1}$ , which is less than the flux in heterogeneous sediment. The characteristic hyporheic residence time is 14.4 days, almost equal to that in heterogeneous sediment.

[26] Solute breakthrough is initially faster in heterogeneous than homogeneous sediment (Figure 6a).  $C_u/C_0$  reaches 50% after 11 h in heterogeneous sediment and after 23 h in homogeneous sediment. Accordingly, the heterogeneous sediment has a greater proportion of short residence times ( $<5 \times 10^4 \text{ s}$ , or 17 h) than homogeneous sediment (Figure 6b). The heterogeneous sediment also has a smaller proportion of intermediate residence times between  $5 \times 10^4 \text{ s}$  (17 h) and  $1 \times 10^6 \text{ s}$  (2 weeks). Again, the tails of both

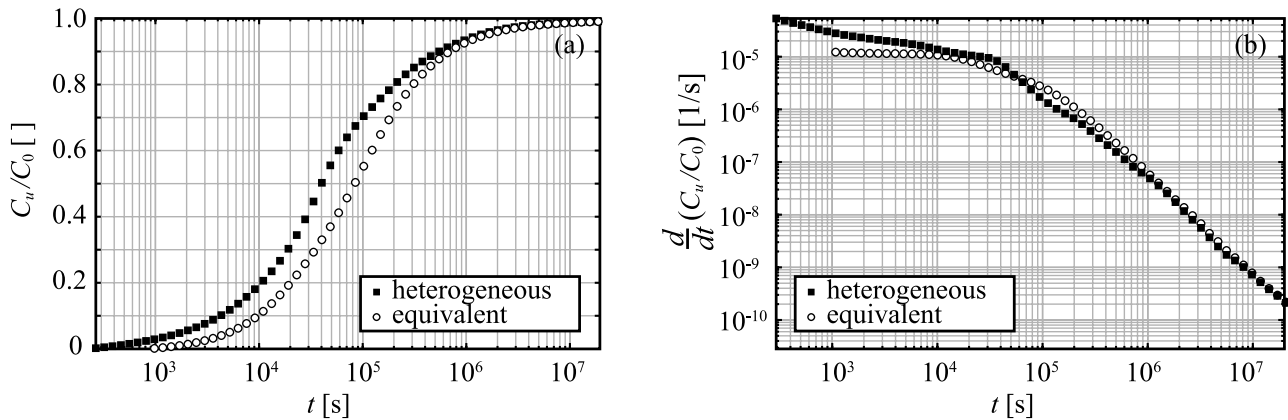


**Figure 6.** (a) Breakthrough curves for the heterogeneous Brazos sediment (black squares) and its homogeneous equivalent sediment (white circles). The breakthrough curve initially climbs faster in heterogeneous sediment. (b) The residence time distribution in heterogeneous sediment strongly emphasizes short residence times. Power law tails have exponents of  $-1.73$  and  $-1.80$  in heterogeneous and equivalent homogeneous sediment, respectively.

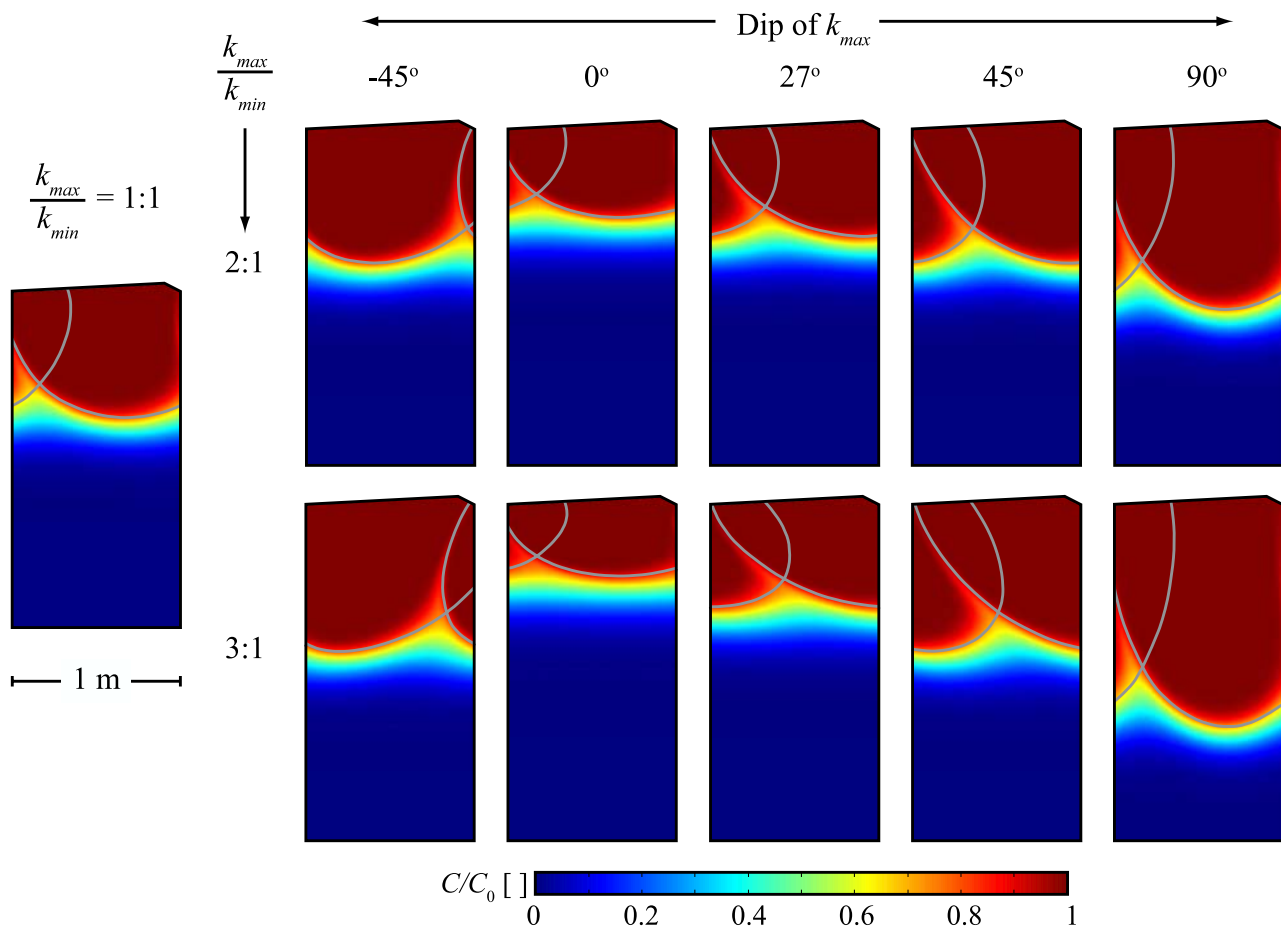


**Figure 7.** Hyporheic zones, delineated by gray streamlines, for various permeability anisotropy ratios ( $k_{\max}/k_{\min}$ ) and directions of  $k_{\max}$ . The hyporheic exchange zone is compressed for horizontal  $k_{\max}$  orientations and elongated for vertical  $k_{\max}$  orientations.

residence time distributions follow a power law until the maximum residence time, approximately  $10^9$  s (30 years).

## 5. Permeability Anisotropy Sensitivity Study

[27] To assess the sensitivity of hyporheic exchange to permeability anisotropy, we also conducted simulations in homogeneous sediment for a range of anisotropic permeability tensors. A given permeability anisotropy tensor may represent cross-bedded sediment with preferential flow parallel to bounding surfaces, slip faces, or angle of bed form climb. For all simulations, the bed form wavelength is 1 m (Table 1), and  $k_{\min}$  is  $10^{-10}$  m<sup>2</sup>, corresponding to very coarse sand [Freeze and Cherry, 1979].

[28] Hyporheic exchange depth varies in response to both the anisotropy ratio ( $k_{\max}/k_{\min}$ ) and orientation of  $k_{\max}$  (Figures 7 and 8). As  $k_{\max}/k_{\min}$  increases, the hyporheic exchange zone deepens if  $k_{\max}$  is near vertical. In contrast, if  $k_{\max}$  is near horizontal, the hyporheic exchange zone becomes more compressed with increasing  $k_{\max}/k_{\min}$ . Notably, the hyporheic exchange depth is sensitive to the dip magnitude of  $k_{\max}$  but insensitive to its upstream or downstream orientation. For example, the hyporheic exchange depths are similar whether the dip of  $k_{\max}$  is  $-45^\circ$  (upstream) or  $+45^\circ$  (downstream) (Figures 7 and 8a).

[29] The mean hyporheic flux is relatively insensitive to the orientation of the permeability tensor (Figure 8b).

Hyporheic flux increases with  $k_{\max}/k_{\min}$ , regardless of  $k_{\max}$  direction. The characteristic hyporheic residence time varies with both  $k_{\max}/k_{\min}$  and the orientation of  $k_{\max}$  (Figure 8c). If  $k_{\max}$  is nearly horizontal, the characteristic hyporheic residence time decreases with increasing  $k_{\max}/k_{\min}$ . Hyporheic flow paths become increasingly shallow and fast. If  $k_{\max}$  is nearly vertical, the characteristic hyporheic residence time remains constant with increasing  $k_{\max}/k_{\min}$ . Deeper flow paths are offset by faster flux rates (compare Figures 8a and 8b for  $k_{\max}$  dip of  $90^\circ$ ).

[30] The  $k_{\max}$  direction impacts the solute breakthrough behavior and shape of the residence time distribution (Figure 9). A horizontal  $k_{\max}$  favors short residence times more than a vertical  $k_{\max}$ : the breakthrough curve initially climbs faster if the dip of  $k_{\max}$  is small (Figure 9a). At late time, the breakthrough curve climbs faster if the dip of  $k_{\max}$  is large. Accordingly, the residence time distribution has a broader tail for vertical  $k_{\max}$  directions (Figure 9b). The tails of the residence time distributions all follow a power law for tens of years.

## 6. Discussion

[31] In both case studies, permeability heterogeneity impacts hyporheic flow paths. In heterogeneous sediment, the flow paths are slightly deeper, and long paths connect nonadjacent bed forms. Hyporheic flow paths in homoge-

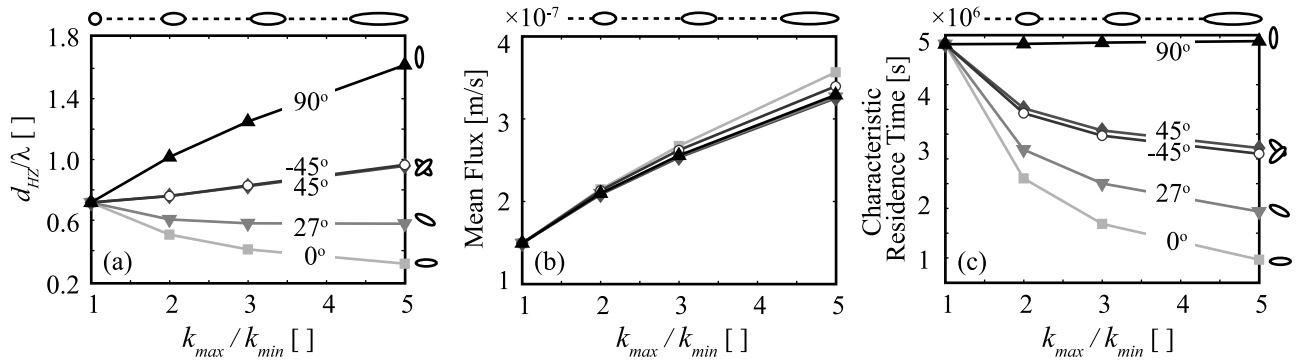


**Figure 8.** (a) Normalized hyporheic exchange depth as a function of  $k_{\max}/k_{\min}$  and dip of  $k_{\max}$ . Ellipses graphically illustrate the permeability anisotropy tensors. (b) Mean hyporheic flux magnitude across the sediment-water interface as a function of  $k_{\max}/k_{\min}$  and dip of  $k_{\max}$ . The rate of hyporheic exchange is insensitive to the orientation of  $k_{\max}$ . (c) Characteristic residence time (exchange depth divided by mean hyporheic flux) as a function of  $k_{\max}/k_{\min}$  and dip of  $k_{\max}$ . The characteristic residence time is most sensitive to  $k_{\max}/k_{\min}$  when  $k_{\max}$  is horizontal.

neous sediment with periodic bed forms only connect adjacent downwelling and upwelling zones. *Woessner* [2000] also presented a case where permeability heterogeneity induced deeper, longer flow paths [see *Woessner*, 2000, Figure 6]. However, some heterogeneous permeability fields may restrict the depth of hyporheic exchange rather than increase it. For example, *Salehin et al.* [2004] found that heterogeneity limited the depth of hyporheic mixing and also decreased residence times. The effective anisotropy of their permeability fields favored lateral flow. Our simulations of hyporheic exchange in anisotropic homogeneous sediment also demonstrate that when the preferential flow direction is horizontal, exchange depths and residence times tend to decrease. A general observation is that permeability heterogeneity increases the complexity of hyporheic exchange paths but may increase or decrease the depth of mixing, depending on the permeability structure.

[32] In spite of the differences between hyporheic flow paths in heterogeneous and equivalent homogeneous sediment, simulations using the homogeneous equivalent permeability tensor predict hyporheic metrics in heterogeneous sediment fairly well. The homogeneous simulation under-

predicted the hyporheic zone depth by 10% for the Massillon Sandstone and by 24% for the Brazos sediment. With respect to the hyporheic flux across the sediment-water interface, the homogeneous simulation overestimated flux by 20% for the Massillon Sandstone and underestimated the flux by 23% for the Brazos sediment.

[33] The implication is that current-bed form interactions primarily control hyporheic metrics in our two case studies. *Cardenas et al.* [2004] presented a dimensionless number for quantifying the relative influence of bed form-current interactions (external forcing) and permeability heterogeneity (internal forcing) on hyporheic exchange:

$$N = \frac{S\sigma_{\ln k}^2 l_z \lambda}{4Ad_{HZ}}. \quad (6)$$

$S$  is the hydraulic gradient in the channel,  $A$  is the amplitude of the pressure field associated with bed form-current interactions,  $\lambda$  is the bed form wavelength,  $d_{HZ}$  is the depth of the hyporheic zone in equivalent homogeneous sediment,  $\sigma_{\ln k}^2$  is the variance of the natural-log permeability field, and  $l_z$  is the vertical correlation length of the permeability field. Large values of  $N$  indicate that permeability heterogeneity

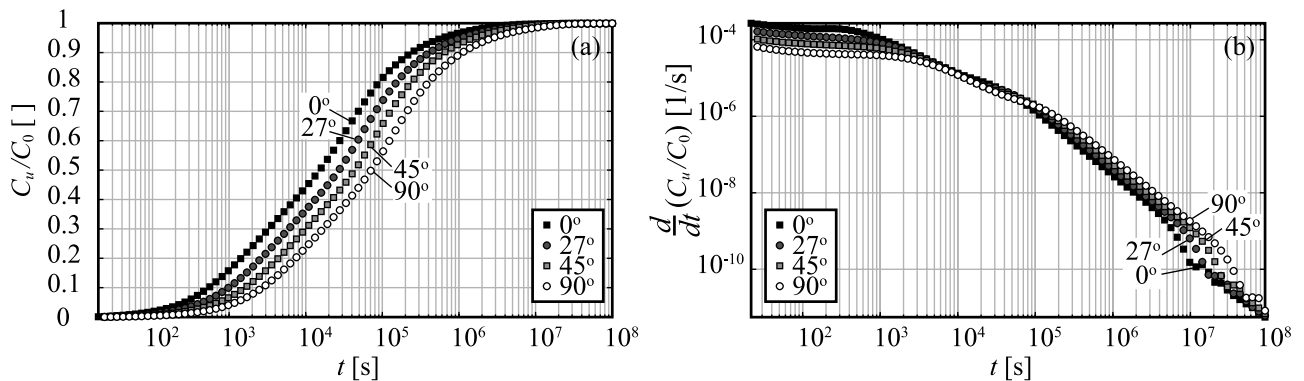


**Figure 9.** (a) Breakthrough curves for homogeneous anisotropic sediment with various  $k_{\max}$  directions.  $k_{\max}/k_{\min}$  is 3.0 in each case. Solute breakthrough is initially slower when  $k_{\max}$  is vertical and hyporheic exchange is deep. (b) Residence time distributions for the four scenarios. The residence time distribution has a broader tail when  $k_{\max}$  is vertical.

**Table 3.** Evaluation of External Versus Internal Forcing Mechanisms for Hyporheic Exchange Through Massillon Sandstone and Brazos Sediment

	$S$ ( $\text{mm m}^{-1}$ )	$\lambda$ (m)	$A$ (mm)	$\sigma_{\text{Ink}}^2$	$l_z$ (m)	$D_{\text{HZ}}$ (m)	$N$
Massillon Sandstone	.194	0.20	.493	.148	.090	.153	.0017
Brazos sediment	.149	0.10	.317	.937	.021	.080	.0029

primarily drives hyporheic exchange, while small values indicate that bed form-current interactions are the primary driver. We calculated  $N$  for the Massillon and Brazos cases (Table 3). For the vertical correlation length ( $l_z$ ), we assumed half the vertical wavelength of the semivariogram hole structure (Table 2).

[34] In both cases,  $N$  is small, suggesting that hyporheic exchange is dominated by bed form-current interactions. For permeability heterogeneity to dominate hyporheic exchange, the permeability correlation length or the variance would need to be much larger, all other factors held constant. If the two case studies examined here are representative of typical correlation lengths and variances for cross bed mesoforms, then mesoscale permeability structure has a limited influence on hyporheic exchange through bed forms. However, larger-scale permeability variations across multiple depositional units such as scroll bars, trough sets, and mud drapes could strongly control hyporheic exchange.

[35] For our two case studies, solute distributions within the sediment were also relatively insensitive to permeability heterogeneity. Figure 10 illustrates vertical concentration profiles at six time intervals for both the heterogeneous Brazos sediment and its homogeneous equivalent sediment. The penetration depths are similar for all times (also compare  $C/C_0$  contours in Figures 2 and 5). Near the sediment-water interface, bed form-current interactions predominantly control hyporheic exchange. The pressure gradients are greatest, and the path lengths are short compared with the length scale of permeability heterogeneity. There-

fore, solute penetration is relatively insensitive to permeability heterogeneity. Deeper in the hyporheic zone, pressure gradients are small, and longer flow paths sample more of the permeability range. Permeability heterogeneity could potentially impact solute transport, but seepage velocities decay logarithmically with depth, so diffusion and pore scale dispersion effectively redistribute solute along flow paths. Therefore, permeability heterogeneity also has a weak influence on solute penetration at depth.

[36] Permeability heterogeneity does impact the distribution of residence times, though all distributions have power law tails. Permeability heterogeneity can increase or decrease the proportion of short or long residence times. In the Massillon Sandstone, permeability heterogeneity increases the proportion of longer residence times (greater than 3 days). In the Brazos sediment, permeability heterogeneity increases the proportion of shorter residence times (less than 17 h). Notably, a different choice in the homogeneous equivalent permeability tensor could improve agreement between heterogeneous and homogeneous residence time distributions at early times or late times, but not both. Because permeability heterogeneity alters the shape of the residence time distribution, no single equivalent permeability tensor can accurately reproduce residence times in heterogeneous sediment.

[37] The permeability distribution near the sediment-water interface appears to strongly influence the residence time behavior. The Massillon Sandstone has a low-permeability bounding surface near the sediment-water interface. On

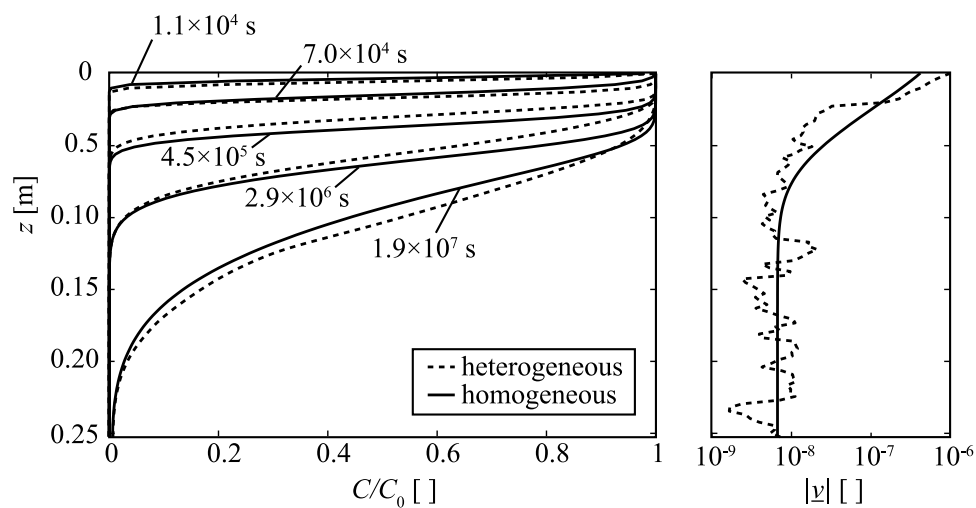


**Figure 10.** Concentration-depth profiles in heterogeneous Brazos sediment (dashed lines) and equivalent homogeneous sediment (solid lines) after introduction of conservative solute to the surface water. Concentration profiles are taken from a vertical line that bisects the central bed form (Figure 5). Solute penetration fronts are similar for both heterogeneous and homogeneous sediment. Because seepage velocity decays logarithmically with depth (right), advection does not strongly influence the deep, late-time penetration of solute into the sediment.

average, the low-permeability surface tends to increase solute residence times. However, the shallowest hyporheic paths near the crests of bed forms pass unimpeded through moderate permeabilities. As a result, the initial solute arrival times at upwelling zones are similar in both the heterogeneous and equivalent homogeneous sediment, but heterogeneity delays solute arrival at later times. Unlike the Massillon Sandstone, the Brazos sediment manifests the full range of permeability near the sediment-water interface. High- and low-permeability zones alternate along the bed form train. In the rightmost bed form, two transitions between upwelling and downwelling occur in a highly permeable zone (Figure 5a). As a result, solute arrives much earlier at upwelling zones in heterogeneous sediment than in homogeneous sediment. At later times however, the breakthrough curve for heterogeneous sediment climbs slowly because deeper hyporheic flow paths inevitably encounter lower permeability regions that delay the travel time. A key conclusion is that subtleties in permeability heterogeneity near the sediment-water interface can lead to measurable differences in solute residence times.

[38] Our numerical experiments have limitations. First, this study considers only two examples of cross-bedded permeability fields. We propose that these cases are nonetheless representative of a wide (yet limited) range of mesoform permeability structures (refer to *Weber* [1982], *Scheibe and Freyberg* [1995], and *Huysmans et al.* [2008] for other examples). Second, we represent three-dimensional bed forms and permeability structures using two-dimensional cross sections. Bed forms tend to exhibit the greatest topographic variation in the streamwise direction, and hydrodynamic grain size sorting processes should similarly produce strong permeability variations in the streamwise direction. We therefore believe the two-dimensional simulations capture the primary behavior of hyporheic flow, though three-dimensional simulations would increase the complexity of flow paths. Third, the domain of our numerical simulations is periodic but only spans three bed forms, which limits the potential length of all hyporheic flow paths to approximately three bed form wavelengths. We suggest, however, that hyporheic flow paths between nonadjacent bed forms weakly influence solute transport and storage for two reasons. First, solute flux along these paths represents a very small portion of the total solute flux through the hyporheic zone. Second, diffusion and pore scale dispersion strongly influence solute transport along these flow paths.

[39] Our two case studies illustrate how cross-bedded permeability structures impact hyporheic exchange and solute transport. Regardless of permeability structure, all flux-weighted residence time distributions follow a power law relationship for tens of years. The key implication is that hyporheic residence times can vary over many orders of magnitude, even in rivers with uniform bed form wavelengths and relatively homogeneous sediment. Permeability heterogeneity may modify the details of the residence time distribution but does not alter the form of the power law tail.

## 7. Conclusions

[40] We have demonstrated in two cases that the permeability structure of cross-bedded sediment can produce long hyporheic exchange paths but only slightly modifies the average exchange depth beneath bed forms. The primary

forcing mechanism is bed form-current interactions. Additionally, conservative solute distributions within the hyporheic zone are relatively insensitive to the permeability heterogeneity of cross-bedded sediment. Therefore, approximating cross-bedded sediment as homogeneous and anisotropic (or even isotropic) is reasonable, if the goal is to understand or describe first-order patterns in hyporheic exchange fluxes and solute distributions within riverbeds. However, this study in no way refutes the impact of large-scale permeability heterogeneity on hyporheic exchange (where correlation lengths greatly exceed the bed form wavelength).

[41] Cross-bedded permeability structures do impact the distribution of hyporheic residence times. Permeability heterogeneity can increase the proportion of short or long residence times. The shape of the residence time distribution appears to be most sensitive to permeability patterns near the sediment-water interface. However, the tails of the residence time distributions follow a power law, regardless of permeability structure. Persistent solute retention in riverbeds does not require large variations in sediment permeability or bed form wavelength.

## Notation

$a$	semivariogram range (L).
$A$	amplitude of dynamic pressure wave ( $M L^{-1} T^{-2}$ ).
$c$	semivariogram sill contribution (dimensionless).
$C$	concentration ( $M L^{-3}$ ).
$C_u$	mean flux-weighted concentration at upwelling zones ( $M L^{-3}$ ).
$C_0$	reference concentration in surface water ( $M L^{-3}$ ).
$\underline{D}$	dispersion tensor ( $L^2 T^{-1}$ ).
$d_{HZ}$	depth of hyporheic exchange zone (L).
$D'_m$	molecular diffusion coefficient in porous media ( $L^2 T^{-1}$ ).
$\underline{h}$	vector lag (L).
$\underline{k}$	permeability tensor ( $L^2$ ).
$l_z$	vertical correlation length of permeability field (L).
$N$	measure of hyporheic exchange forcing mechanisms (dimensionless).
$P$	total potential ( $M L^{-1} T^{-2}$ ).
$Pe$	Peclet number (dimensionless).
$S$	channel hydraulic gradient (dimensionless).
$t$	time (T).
$\underline{v}$	seepage velocity ( $L T^{-1}$ ).
$x$	longitudinal coordinate (L).
$y(\underline{u})$	sample attribute value at location $\underline{u}$ (dimensionless).
$z$	vertical coordinate (L).
$\alpha_L$	longitudinal dispersivity (L).
$\alpha_T$	transverse dispersivity (L).
$\Gamma$	semivariogram structure (dimensionless).
$\gamma$	semivariogram (dimensionless).
$\lambda$	bed form wavelength (L).
$\mu$	dynamic viscosity ( $M L^{-1} T^{-1}$ ).
$\sigma_{lnk}^2$	variance of natural-log permeability field (dimensionless).

[42] **Acknowledgments.** We thank Vincent Tidwell for the use of the Massillon Sandstone permeability data set and Gary Kocurek for his photograph of Brazos River sediment. We also thank Sanjay Srinivasan for his assistance in geostatistical analysis. Comments from Editor Scott Tyler, Associate Editor Olaf Cirpka, and three anonymous reviewers are

greatly appreciated. This research was funded by the American Chemical Society-Petroleum Research Fund (46655-G8).

## References

- Allen, J. R. (1971), A theoretical and experimental study of climbing-ripple cross-lamination, with a field application to the Uppsala Esker, *Geogr. Ann., Ser. A*, 53(3/4), 157–187, doi:10.2307/520787.
- Boano, F., C. Camporeale, R. Revelli, and L. Ridolfi (2006), Sinuosity-driven hyporheic exchange in meandering rivers, *Geophys. Res. Lett.*, 33, L18406, doi:10.1029/2006GL027630.
- Boano, F., A. I. Packman, A. Cortis, R. Revelli, and L. Ridolfi (2007), A continuous time random walk approach to the stream transport of solutes, *Water Resour. Res.*, 43, W10425, doi:10.1029/2007WR006062.
- Boulton, A. J. (2007), Hyporheic rehabilitation in rivers: Restoring vertical connectivity, *Freshwater Biol.*, 52, 632–650, doi:10.1111/j.1365-2427.2006.01710.x.
- Brunke, M., and T. Gonser (1997), The ecological significance of exchange processes between rivers and groundwater, *Freshwater Biol.*, 37, 1–33, doi:10.1046/j.1365-2427.1997.00143.x.
- Cardenas, M. B. (2007), Potential contribution of topography-driven regional groundwater flow to fractal stream chemistry: Residence time distribution analysis of Tóth flow, *Geophys. Res. Lett.*, 34, L05403, doi:10.1029/2006GL029126.
- Cardenas, M. B., and J. L. Wilson (2007), Dunes, turbulent eddies, and interfacial exchange with permeable sediments, *Water Resour. Res.*, 43, W08412, doi:10.1029/2006WR005787.
- Cardenas, M. B., J. L. Wilson, and V. A. Zlotnik (2004), Impact of heterogeneity, bed forms, and stream curvature on subchannel hyporheic exchange, *Water Resour. Res.*, 40, W08307, doi:10.1029/2004WR003008.
- Cardenas, M. B., J. L. Wilson, and R. Haggerty (2008), Residence time of bedform-driven hyporheic exchange, *Adv. Water Resour.*, 31, 1382–1386, doi:10.1016/j.advwatres.2008.07.006.
- COMSOL AB (2006), COMSOL Multiphysics User's Guide, COMSOL AB, Burlington, Mass.
- Deutsch, C. V., and A. G. Journel (1998), *GSLIB: Geostatistical Software Library and User's Guide*, 2 ed., 369 pp., Oxford Univ. Press, New York.
- Durlafsky, L. J. (1991), Numerical calculation of equivalent grid block permeability tensors for heterogeneous porous media, *Water Resour. Res.*, 27(5), 699–708, doi:10.1029/91WR00107.
- Elliott, A. H., and N. H. Brooks (1997a), Transfer of nonsorbing solutes to a streambed with bed forms: Laboratory experiments, *Water Resour. Res.*, 33(1), 137–151, doi:10.1029/96WR02783.
- Elliott, A. H., and N. H. Brooks (1997b), Transfer of nonsorbing solutes to a streambed with bed forms: Theory, *Water Resour. Res.*, 33(1), 123–136, doi:10.1029/96WR02784.
- Fluent Inc. (2006), *FLUENT 6.3 User's Guide*, Fluent Inc., Lebanon, N. H.
- Freeze, R. A., and J. A. Cherry (1979), *Groundwater*, 604 pp., Prentice-Hall, Englewood Cliffs, N. J.
- Gray, H. H. (1956), Petrology of the Massillon Sandstone at the type locality, *Ohio J. Sci.*, 56(3), 138.
- Greig, S. M., D. A. Sear, and P. A. Carling (2007), A review of factors influencing the availability of dissolved oxygen to incubating salmonid embryos, *Hydro. Processes*, 21, 323–334, doi:10.1002/hyp.6188.
- Haggerty, R., S. M. Wondzell, and M. A. Johnson (2002), Power-law residence time distribution in the hyporheic zone of a 2nd-order mountain stream, *Geophys. Res. Lett.*, 29(13), 1640, doi:10.1029/2002GL014743.
- Hakenkamp, C. C., A. Morin, and D. L. Strayer (2002), The functional importance of freshwater meiofauna, in *Freshwater Meiofauna: Biology and Ecology*, edited by A. L. R. S. D. Rundle and J. M. Schmid-Araya, pp. 321–335, Backhuys, Leiden, Netherlands.
- Harvey, J. W., and K. E. Bencala (1993), The effect of streambed topography on surface-subsurface water exchange in mountain catchments, *Water Resour. Res.*, 29(1), 89–98, doi:10.1029/92WR01960.
- Hester, E. T., and M. W. Doyle (2008), In-stream geomorphic structures as drivers of hyporheic exchange, *Water Resour. Res.*, 44, W03417, doi:10.1029/2006WR005810.
- Huysmans, M., L. Peeters, G. Moermans, and A. Dassargues (2008), Relating small-scale sedimentary structures and permeability in a cross-bedded aquifer, *J. Hydrol.*, 361, 41–51, doi:10.1016/j.jhydrol.2008.07.047.
- Marion, A., A. I. Packman, M. Zaramella, and A. Bottacin-Busolin (2008), Hyporheic flows in stratified beds, *Water Resour. Res.*, 44, W09433, doi:10.1029/2007WR006079.
- Peterson, E. W., and T. B. Sickbert (2006), Stream water bypass through a meander neck, laterally extending the hyporheic zone, *Hydrogeol. J.*, 14(8), 1443–1451, doi:10.1007/s10040-006-0050-3.
- Renard, P., and G. de Marsily (1997), Calculating equivalent permeability: A review, *Adv. Water Resour.*, 50(5–6), 253–278.
- Ritzi, R. W., Z. Dai, D. F. Dominic, and Y. N. Rubin (2004), Spatial correlation of permeability in cross-stratified sediment with hierarchical architecture, *Water Resour. Res.*, 40, W03513, doi:10.1029/2003WR002420.
- Salehin, M., A. I. Packman, and M. Paradis (2004), Hyporheic exchange with heterogeneous streambeds: Laboratory experiments and modeling, *Water Resour. Res.*, 40, W11504, doi:10.1029/2003WR002567.
- Scheibe, T. D., and D. L. Freyberg (1995), Use of sedimentological information for geometric simulation of natural porous media structure, *Water Resour. Res.*, 31(12), 3259–3270, doi:10.1029/95WR02570.
- Schmidley, E. B. (1986), The sedimentology, paleogeography and tectonic setting of the Pennsylvanian Massillon Sandstone in east-central Ohio, M.S. thesis, Univ. of Akron, Akron, Ohio.
- Stanford, J. A., and J. V. Ward (1988), The hyporheic habitat of river ecosystems, *Nature*, 335, 64–66, doi:10.1038/335064a0.
- Thibodeaux, L. J., and J. D. Boyle (1987), Bedform-generated convective transport in bottom sediment, *Nature*, 325, 341–343, doi:10.1038/325341a0.
- Tidwell, V. C., and J. L. Wilson (2000), Heterogeneity, permeability patterns, and permeability upscaling: Physical characterization of a block of Massillon Sandstone exhibiting nested scales of heterogeneity, *SPE Reservoir Eval. Eng.*, 3(4), 283–291, doi:10.2118/65282-PA.
- Tidwell, V. C., and J. L. Wilson (2002), Visual attributes of a rock and their relationship to permeability: A comparison of digital image and mini-permeameter data, *Water Resour. Res.*, 38(11), 1261, doi:10.1029/2001WR000932.
- Vaux, W. G. (1968), Intragravel flow and interchange of water in a streambed, *Fish. Bull.*, 66, 479–489.
- Wagner, F. H., and G. Bretschko (2002), Interstitial flow through preferential flow paths in the hyporheic zone of the Oberer Seebach, Austria, *Aquat. Sci.*, 64(3), 307–316, doi:10.1007/s00027-002-8075-8.
- Weber, K. J. (1982), Influence of common sedimentary structures on fluid flow in reservoir models, *JPT J. Pet. Technol.*, 34, 665–672, doi:10.2118/9247-PA.
- Woessner, W. W. (2000), Stream and fluvial plain ground water interactions: Rescaling hydrogeologic thought, *Ground Water*, 38(3), 423–429, doi:10.1111/j.1745-6584.2000.tb00228.x.
- Worman, A., A. I. Packman, L. Marklund, J. W. Harvey, and S. H. Stone (2006), Exact three-dimensional spectral solution to surface-groundwater interactions with arbitrary surface topography, *Geophys. Res. Lett.*, 33, L07402, doi:10.1029/2006GL025747.

M. B. Cardenas and A. H. Sawyer, Department of Geological Sciences, University of Texas at Austin, 1 University Station C9000, Austin, TX 78712, USA. (asawyer@mail.utexas.edu)